

# DoppDrive: Doppler-Driven Temporal Aggregation for Improved Radar Object Detection

Yuval Haitman\* and Oded Bialer\*  
General Motors, Technical Center Israel

haitman@post.bgu.ac.il, oded.bialer8@gmail.com

## Abstract

Radar-based object detection is essential for autonomous driving due to radar's long detection range. However, the sparsity of radar point clouds, especially at long range, poses challenges for accurate detection. Existing methods increase point density through temporal aggregation with ego-motion compensation, but this approach introduces scatter from dynamic objects, degrading detection performance. We propose DoppDrive, a novel Doppler-Driven temporal aggregation method that enhances radar point cloud density while minimizing scatter. Points from previous frames are shifted radially according to their dynamic Doppler component to eliminate radial scatter, with each point assigned a unique aggregation duration based on its Doppler and angle to minimize tangential scatter. DoppDrive is a point cloud density enhancement step applied before detection, compatible with any detector, and we demonstrate that it significantly improves object detection performance across various detectors and datasets. Our project page: <https://yuvalhg.github.io/DoppDrive/>

## 1. Introduction

Radar plays an important role in autonomous driving and active safety systems due to its capability to provide detection at long range [17, 24, 43]. While some approaches use neural networks to detect objects directly from the radar's reflection intensity tensor spectrum [11, 16, 19, 44, 45], spanning spatial and Doppler domains, this low-level data is not always accessible. When available, it requires substantial communication bandwidth, memory, and computational resources to process. A more efficient alternative is object detection from radar point cloud data [14, 22, 27–29, 31, 38], where the point cloud is generated by filtering high-probability reflection points from the intensity ten-

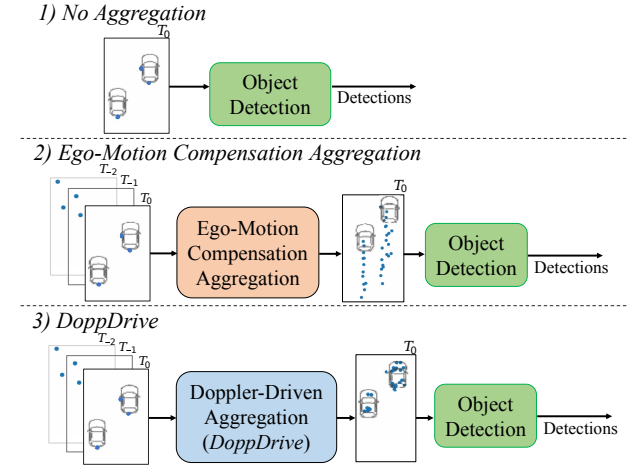


Figure 1. **Object detection with different input point clouds.** (1) single frame, highly sparse point cloud, (2) temporally aggregated with ego-motion compensation—scattered points from dynamic objects, (3) Doppler-driven aggregation—dense points with minimal scatter, enhancing object detection.

sor spectrum [32]. This paper focuses on object detection using radar point clouds, a method conceptually similar to LIDAR-based detection but with critical distinctions.

One key difference between radar and LIDAR point clouds is radar's much lower density, due to its lower angular resolution and longer wavelength [15]. This sparsity increases with distance, resulting in only a few reflections from distant objects, making it challenging to distinguish true objects from noise and accurately detect their shape, orientation, and size. As objects' reflection points vary with changes in the relative position between objects and the radar, a common approach to increasing point cloud density and improving object detection is to aggregate point clouds from multiple frames over a short duration (about 0.5 seconds), applying ego-motion compensation and adding a timestamp to each point [22, 28, 29, 33, 38, 42]. While this method aligns reflections from static objects, the unknown velocities of dynamic objects cause significant scatter in the

\*Both authors contributed equally to this work.

Both authors are with General Motors, Yuval Haitman is also with the School of Electrical and Computer Engineering in Ben Gurion University of the Negev.

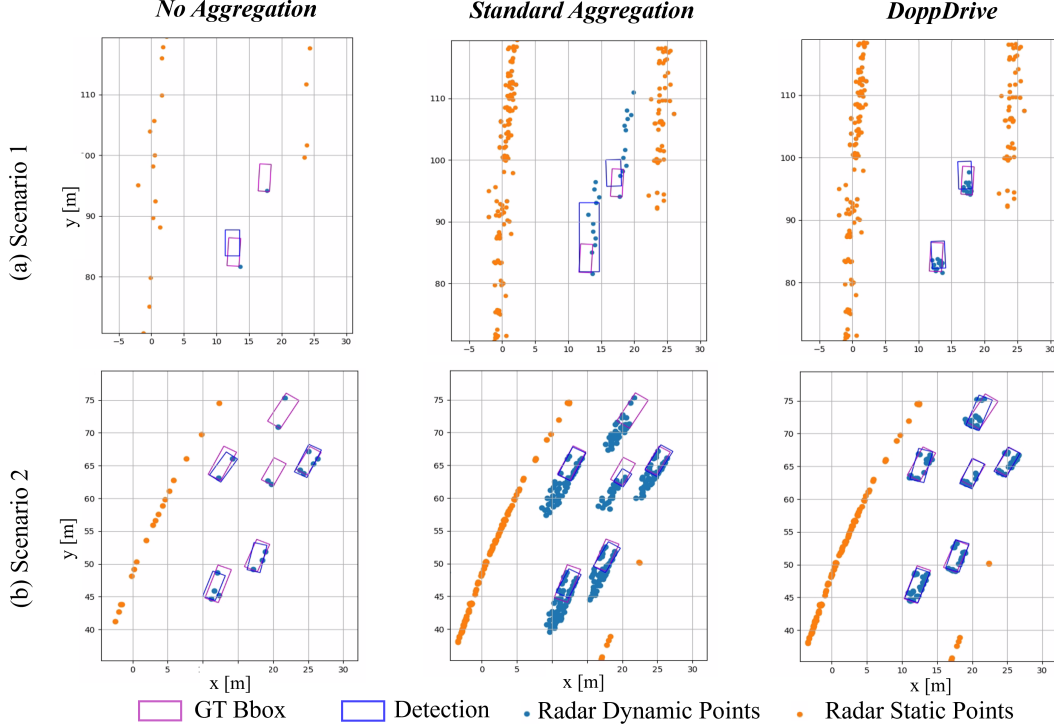


Figure 2. **Qualitative examples demonstrating *DoppDrive* in two scenarios:** the upper row (a) from the aiMotive dataset [25] and the lower row (b) from *LRR-Sim* (Sec. 5). Columns show: (left) Sparse point cloud without aggregation, leading to missed detections; (center) Aggregation with ego-motion compensation, causing scattered points around dynamic objects and inaccuracies in object size and position; (right) *DoppDrive* enhances density around dynamic objects (blue points) with minimal scatter, improving detection accuracy. Detections are obtained using SMF [22].

aggregated data, limiting performance.

Developing methods to increase radar point cloud density without introducing scatter could greatly improve object detection, especially for long-range radar, which must detect objects at distances of up to 300m for high-speed autonomous driving [1, 2, 5, 23, 34, 36, 48]. However, current automotive radar datasets are limited to 175m, primarily due to the difficulty of obtaining accurate annotations at greater distances. At these ranges, radar points become very sparse, and the LIDAR and camera sensors typically used for annotation struggle to detect objects accurately. A dataset extending beyond 175m with precise annotations could significantly advance research in long-range radar detection.

Another key distinction between radar and LIDAR is radar’s Doppler measurement, which captures the radial velocity of each reflection point relative to the radar. The Doppler measurement consists of two components: the *ego-speed Doppler* component (due to ego-vehicle motion) and the *dynamic Doppler* component (due to object motion). The ego-speed component can be calculated from the ego-vehicle’s velocity [38], which is either obtained from auxiliary sensors like GPS-INS or odometers [3, 9, 13, 35] or can be estimated from the radar’s point cloud Doppler in-

formation [4, 18, 30, 38]. Previous work on radar-based object detection incorporates Doppler information as an additional input feature for each point, using object detection networks originally designed for LIDAR point clouds with the added Doppler feature [22, 28, 29, 38]. Removing the ego-speed Doppler component from the Doppler measurement has been shown to aid object detection [28, 38], as it enables the residual Doppler to indicate whether a point reflects a static (zero residual Doppler) or dynamic (non-zero residual Doppler) object, helping the neural network learn distinct features for detection. However, exploring additional ways to leverage the dynamic Doppler component information to enhance object detection yet remains a valuable and important direction for research.

This paper introduces *DoppDrive*, a Doppler-driven temporal aggregation method that uses Doppler information in a novel way to enhance radar point cloud prior to object detection. *DoppDrive* increases point cloud density while minimizing scatter in reflections from dynamic objects. By aligning points from previous frames to the current frame along the radial direction based on dynamic Doppler velocity, *DoppDrive* eliminates range scatter. Additionally, it mitigates tangential spread by setting each point’s aggregation duration based on its specific Doppler and angle, result-

ing in dynamic aggregation durations per point rather than a fixed duration for all.

Fig. 1 shows the high-level concept of *DoppDrive* compared to standard aggregation with ego-vehicle motion compensation and no aggregation. Fig. 2 presents qualitative examples of these point clouds, demonstrating *DoppDrive*'s increased density with minimal dispersion. As we will show, this enhancement improves object detection performance. *DoppDrive* is compatible with any point cloud detection network, and we validate its performance improvements across four detectors and three datasets.

To address the shortage of datasets for testing methods on sparse radar point clouds beyond 200m, we introduce a new dataset, *LRR-Sim*, as part of this work. *LRR-Sim* simulates a long-range automotive radar in highway scenarios, providing annotated point clouds up to 300m. We use it to evaluate our method alongside reference approaches at extended detection ranges. The dataset is publicly released to support future research in long-range radar perception.

The main contributions of the paper are as follows:

1. A novel Doppler-driven temporal aggregation method that increases the density of radar point clouds while minimizing spatial scattering of points from dynamic objects, thereby enhancing object detection performance.
2. The release of *LRR-Sim*, a long-range automotive radar dataset with sparse point clouds from extended detection ranges and precise annotations up to 300m. It is generated by radar simulation to address the challenge of obtaining accurate long-distance annotations. The dataset is publicly available and serves as a valuable resource for advancing radar-based long-range detection.

## 2. Related Work

### 2.1. Object Detection From Radar Point Cloud

Various methods exist for radar point cloud object detection. Several methods leverage PointPillars [20] for radar detection [22, 28, 38, 40, 47], while NVRadarNet [29] uses 2D convolution with a Feature Pyramid Network [21] in bird's-eye view, and K-Radar [27] applies 3D sparse convolution. RADial [31] utilizes PIXOR [41], and Radar-transformer [6] employs a transformer architecture for radar detection. Additional approaches include graph convolution [14, 37] and hybrid of point-based and grid-based networks [39]. All radar point cloud detection networks face challenges due to point cloud sparsity, which limits performance. Increasing point cloud density can enhance their effectiveness, which is the focus of our work.

### 2.2. Radar Datasets

Radar point cloud datasets are characterized by detection range and angular resolution, where higher resolution results in a denser point cloud, while a longer detection range

reduces point density.

Publicly available low-resolution radar datasets with object annotations include nuScenes [8], covering urban, residential, and industrial areas; PixSet [10], focused on high-density urban environments, both limited to object ranges below 80m; and aiMotive [25], which extends detection up to 175m in urban and highway environments. High-resolution radar datasets with object annotations include K-Radar [27], which has limited Doppler speed measurements; View-of-Delft [28], with a maximum detection range of 50m; Astyx [26], which is relatively small; TJ4DRadSet [46], with a detection range up to 90m; and RADial [31], which has a 103m range and captures data from highway, country-side and city driving.

In this paper, we evaluate our method performance on the aiMotive and RADial datasets, representing low- and high-resolution radars with relatively long detection ranges. Additionally, we introduce a new dataset for long-range radar detection, with point clouds and objects up to 300m, significantly extending the range of existing datasets (see Sec. 5).

### 2.3. Ego-Vehicle Velocity

Ego-vehicle velocity is typically obtained from a GPS-INS sensor or vehicle odometers [3, 9, 13, 35]. Alternatively, it can be estimated from radar point clouds by identifying static objects (e.g., guardrails, buildings, poles, ground) via Doppler clustering. The Doppler of each static point represents a different radial component of the vehicle's velocity. Thus, Doppler measurements from static reflections can be expressed as a function of point angles and ego-vehicle velocity, allowing the velocity to be resolved [4, 18, 30, 38].

## 3. Background: Doppler Components

This section provides background material used in deriving our method in Sec. 4. In automotive scenarios, the variation in height over short aggregation durations is relatively small. Thus, throughout this paper, we assume zero vertical velocity and focus only on longitudinal and lateral velocity. Fig. 3 shows a reflection point in top view relative to the radar, where the point's angle to the radar is  $\theta$  and its heading angle is  $\alpha$  with speed  $s$  (blue arrow). The radial and tangential velocity components are  $v$  and  $u$  (green and red arrows), respectively, and are given by:

$$v = s \cos(\theta + \alpha), \quad (1)$$

$$u = s \sin(\theta + \alpha). \quad (2)$$

Solving for  $s$  in Eq. (1) and substituting into Eq. (2), we obtain:

$$u = v \tan(\theta + \alpha). \quad (3)$$

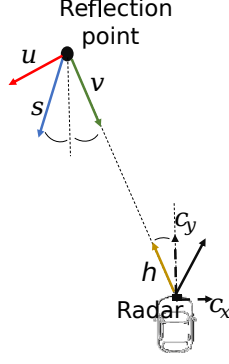


Figure 3. **Scenario with a dynamic reflection point and a moving radar.** The reflection point's radial and tangential velocity components are  $v$  and  $u$ , respectively. The Doppler measurement is the sum of the radial velocity  $v$  of the dynamic object (dynamic Doppler component) and the radial velocity due to ego-vehicle motion  $h$  (ego-speed Doppler component).

In Fig. 3, the radar-equipped host vehicle moves along the black arrow with speed vector  $\mathbf{c} = [c_x, c_y]$ . The projection of  $\mathbf{c}$  onto the reflection point's direction is denoted by  $h$ , and calculated by:

$$h = c_x \sin(\theta) + c_y \cos(\theta). \quad (4)$$

The radar measures Doppler frequency, which is converted to velocity units. The point's Doppler measurement, denoted by  $d$ , is the relative radial velocity between the radar and the point, accounting for both the point and ego-vehicle motions:  $d = v + h$ , where  $v$  is the dynamic Doppler component (point's radial velocity) and  $h$  is the ego-speed Doppler component.

The speed of the ego vehicle  $\mathbf{c}$  can be obtained from a GPS-INS sensor or estimated from the radar point cloud (see Sec. 2.3). Given  $\mathbf{c}$ , we calculate  $h$  for each point from Eq. (4) and obtain its dynamic Doppler component as  $v = d - h$ . In Sec. 4, we represent the reflection point's velocity vector using the radial component  $v$  (dynamic Doppler component) and the tangential component from Eq. (3).

#### 4. Doppler-Driven Temporal Aggregation

Our point cloud aggregation algorithm enhances reflection point density to improve object detection by combining radar point clouds from previous frames with those of the current frame, as shown in Fig. 1. This aggregation adjusts for both the ego-vehicle's motion and the movement of dynamic objects between frames, using Doppler information from the radar point clouds.

Fig. 4 illustrates the proposed Doppler-Driven aggregation method. In the bird's-eye-view scenario in Fig. 4(a), the radar-equipped host vehicle (bottom) and an oncoming

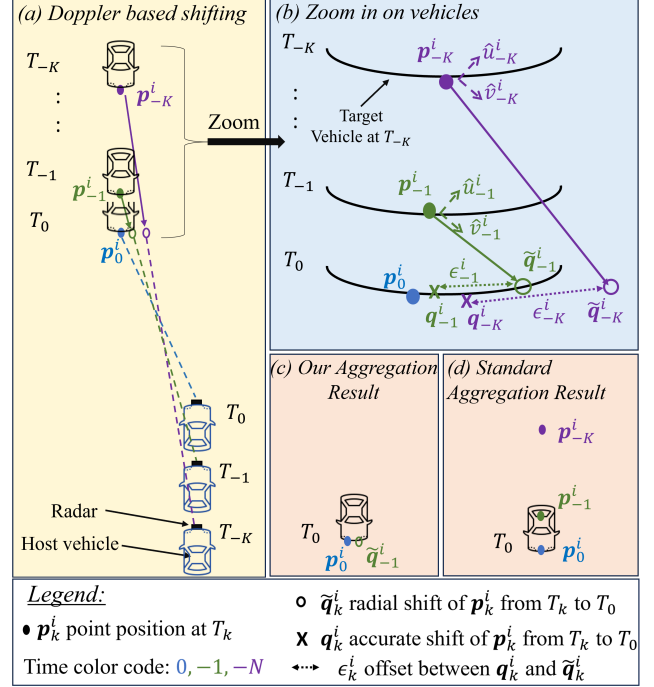


Figure 4. **Overview of the Doppler-driven temporal aggregation method.** (a) Top view of the scenario with the radar-equipped host vehicle and a dynamic vehicle moving toward each other. Points from previous frames  $T_{-1}$  and  $T_{-K}$  are aggregated with the current frame  $T_0$ , compensating for the dynamic vehicle's motion by shifting points along the radial direction based on their dynamic Doppler measurement. (b) Zoom-in on (a), showing the accurate shift  $\mathbf{q}_k^i$  vs. the approximated shift  $\tilde{\mathbf{q}}_k^i$ , with resulting offset distance  $\epsilon_k^i$ . (c) Result of our aggregation method, showing denser reflection points with minimal disparity where the aggregation duration of  $\tilde{\mathbf{q}}_k^i$  yields an expected offset beyond the tolerated limit, so it is discarded. (d) Result of standard aggregation, showing significant scatter in the aggregated points.

dynamic vehicle approach each other. Frame times are denoted by  $T_k$ , where  $k = 0$  is the current frame and negative  $k$  values indicate earlier frames. The figure shows both vehicles at three frames: the current frame  $T_0$ , one prior frame  $T_{-1}$ , and  $K$  frames back at  $T_{-K}$ . Let  $\mathbf{p}_k^i$  represent the 3D position  $(x, y, z)$  of the  $i$ -th reflection point at frame  $T_k$ . In this example, a single reflection point from the approaching vehicle appears in each frame, represented as  $\mathbf{p}_{-K}^i$ ,  $\mathbf{p}_{-1}^i$ , and  $\mathbf{p}_0^i$ , shown in top view as solid circles in purple, green, and blue, respectively, in Fig. 4. Throughout this section, all point positions are referenced to a *unified coordinate system*, such as the radar's coordinate system at  $T_0$ . This is achieved by transforming all points to  $T_0$  coordinates, using ego-vehicle motion data from external sensors or estimating it from the radar point cloud (see Sec. 2.3).

The radial direction between each reflection point,  $\mathbf{p}_k^i$ , and the radar position at frame time  $T_k$  is shown as dashed



lines in Fig. 4(a). Our key idea is to compensate for the shift in reflection points from previous frames to the current frame caused by the dynamic vehicle's motion, using the dynamic Doppler measurement, which represents the dynamic vehicle's radial velocity. Each previous point is shifted along its radial direction according to its dynamic Doppler measurement, as illustrated by solid arrows in Fig. 4(a), with arrow colors matching the points. The adjusted positions, marked by hollow circles in corresponding colors, correct for radial motion but still leave a tangential offset. To mitigate this, we limit each point's aggregation duration, as explained further below.

To further explain our aggregation method, we refer to Fig. 4(b), which provides a zoomed-in view of Fig. 4(a). Let  $\mathbf{q}_k^i$  be the position of  $\mathbf{p}_k^i$  after shifting it accurately to the current time frame  $T_0$  based on the dynamic object's precise velocity. These shifted points are marked with an 'x' in Fig. 4(b), with colors matching their original positions. We neglect any slight motion in height during the short integration interval and approximate zero velocity in this dimension. Thus, the velocity vector that accurately shifts  $\mathbf{p}_k^i$  has only radial and tangential components,  $v_k^i$  and  $u_k^i$ , respectively, so that:

$$\mathbf{q}_k^i = \mathbf{p}_k^i + v_k^i \hat{\mathbf{v}}_k^i (T_0 - T_k) + u_k^i \hat{\mathbf{u}}_k^i (T_0 - T_k), \quad (5)$$

where  $\hat{\mathbf{v}}_k^i$  and  $\hat{\mathbf{u}}_k^i$  are 3D unit vectors in the radial and tangential directions on a plane (zero in height), as indicated by dashed arrows in Fig. 4(b) (with further explanation in Sec. 3). In Eq. (5), the radial velocity  $v_k^i$  is known from the dynamic Doppler measurement, while the tangential velocity  $u_k^i$  is unknown. Therefore, we approximate the shifted position  $\mathbf{q}_k^i$  by only compensating for the radial shift. This approximation,  $\tilde{\mathbf{q}}_k^i$ , is given by:

$$\mathbf{q}_k^i \approx \tilde{\mathbf{q}}_k^i = \mathbf{p}_k^i + v_k^i \hat{\mathbf{v}}_k^i (T_0 - T_k). \quad (6)$$

The shifted points,  $\tilde{\mathbf{q}}_{-K}^i$  and  $\tilde{\mathbf{q}}_{-1}^i$ , from times  $T_{-K}$  and  $T_{-1}$ , are shown in Fig. 4(b), with green and purple hollow circles, respectively. The distance offset between the accurate and approximated positions is given by:

$$\epsilon_k^i = \|\mathbf{q}_k^i - \tilde{\mathbf{q}}_k^i\| = |u_k^i| (T_0 - T_k). \quad (7)$$

By substituting Eq. (3) into Eq. (7) we have that

$$\epsilon_k^i = |v_k^i| (T_0 - T_k) \tan(\theta_k^i + \alpha_k^i), \quad (8)$$

where  $\theta_k^i$ , and  $\alpha_k^i$ , are the  $i^{th}$  reflection point angle and heading direction at frame time  $T_k$ . The offsets  $\epsilon_{-K}^i$  and  $\epsilon_{-1}^i$  for points  $\tilde{\mathbf{q}}_{-K}^i$  and  $\tilde{\mathbf{q}}_{-1}^i$  are indicated by dotted lines in Fig. 4(b) with purple and green colors, respectively.

The average offset is obtained by taking the expectation of Eq. (8) with respect to  $\alpha_k^i$ . We set a pre-defined limit to the tolerated average offset, denoted by  $\mathcal{D}$ , such that

$$\mathbb{E}_{\alpha_k^i} [\epsilon_k^i] = |v_k^i| (T_0 - T_k) g(\theta_k^i) \leq \mathcal{D} \quad (9)$$

where

$$g(\theta_k^i) = \mathbb{E}_{\alpha_k^i} [\tan(\theta_k^i + \alpha_k^i)] = \int_{-\pi/2}^{\pi/2} \tan(\theta_k^i + \alpha) f_{\alpha_k^i}(\alpha) d\alpha \quad (10)$$

and  $f_{\alpha_k^i}(\alpha)$  is the distribution of the dynamic vehicle orientation angle  $\alpha$  (shown in Fig. 3), which can be empirically derived from an annotated dataset or approximated by a Laplace distribution. For further details on calculating of  $g(\theta_k^i)$ , please refer to Appendix D.

By rearranging terms in Eq. (9) we can express a limit on the aggregation duration per each point, depending on its Doppler and angle, that will ensure the average shift offset will be below the predefined tolerance  $\mathcal{D}$  as follows:

$$T_0 - T_k \leq \frac{\mathcal{D}}{|v_k^i| g(\theta_k^i)}. \quad (11)$$

In aggregating points from previous frames to the current time, we include only those with an aggregation duration ( $T_0 - T_k$ ) that satisfy Eq. (11), ensuring the average shift offset remains within the specified tolerance  $\mathcal{D}$ . Note that as a result, each point has a specific aggregation duration, which differs from conventional methods that use a fixed aggregation duration to all points.

In the illustrated example of Fig. 4(b), the aggregation duration  $T_0 - T_{-1}$  results in an offset  $\epsilon_{-1}^i$  for  $\tilde{\mathbf{q}}_{-1}^i$  that is below  $\mathcal{D}$ , so it is included in the aggregation at  $T_0$ . In contrast,  $\epsilon_{-K}^i$  for  $\tilde{\mathbf{q}}_{-K}^i$  exceeds  $\mathcal{D}$ , hence this point is *excluded*. The final aggregated result is shown in Fig. 4(c), this includes the current frame point and the previous frame point with low disparity. For comparison, Fig. 4(d) shows conventional aggregation without dynamic motion compensation, resulting in point spread along both radial and tangential directions. In contrast, our method increases the points density with minimal tangential spread and no radial spread.

While Fig. 4 illustrates a single reflection point from one dynamic object per time instance, the method applies to multiple reflection points from objects with varying velocities, including static ones. Each point is independently shifted along its radial direction to the ego-vehicle based on its dynamic Doppler measurement, with static points (zero dynamic Doppler) remaining unchanged. Fig. 2 demonstrates *DoppDrive*'s effectiveness in complex scenarios with multiple vehicles at different speeds. The pseudocode for the proposed Doppler-Driven aggregation algorithm is provided in Algorithm 1.

## 4.1. Object Detection

The *DoppDrive* point cloud aggregation, as described in Algorithm 1, operates frame by frame. For each new frame, a set of aggregated points,  $\mathcal{Q}$ , is computed in a sliding window fashion, combining points from the current frame and previous frames. For object detection, each point in  $\mathcal{Q}$  is

---

**Algorithm 1** Doppler-Driven Aggregation (*DoppDrive*)

---

```
1: Setting: Tolerated aggregation shift error,  $\mathcal{D}$ 
2: Input:
  • Set of points  $p_k^i$ , with their dynamic Doppler velocity  $v_k^i$ , radial unit vector  $\hat{v}_k^i$ , angle  $\theta_k^i$ , and frame time  $T_k$ 
  • Indices:  $i \in \{0, 1, \dots, N\}$  (points),  $k \in \{0, -1, \dots, -K\}$  (frame times)
3: Output: Aggregated set of shifted points  $\mathcal{Q}$  across frame times  $T_0, T_{-1}, \dots, T_{-K}$ 
4: Initialize: Aggregation set  $\mathcal{Q} \leftarrow \emptyset$ 
5: for  $k = -K$  to  $0$  do
6:   for  $i = 0$  to  $N$  do
7:     Calculate  $g(\theta_k^i)$  from Eq. (10)
8:     if  $T_0 - T_k \leq \frac{\mathcal{D}}{|v_k^i|g(\theta_k^i)}$  then
9:       Shift point:  $\tilde{q}_k^i = p_k^i + v_k^i \hat{v}_k^i (T_0 - T_k)$ 
10:      Append  $\tilde{q}_k^i$  to aggregation set  $\mathcal{Q}$ 
11:     else
12:       Discard point  $p_k^i$ 
13:     end if
14:   end for
15: end for
16: return Aggregated set of points  $\mathcal{Q}$ 
```

---

represented by six features: its 3D position  $(x, y, z)$  in the radars coordinate system of the current frame time  $T_0$ , the dynamic Doppler component, reflection intensity, and the time frame index  $k$  when the point was originally received. Any object detection network designed for point clouds can then be used to detect objects from the aggregated points of each frame, utilizing these input features.

## 5. Long Range Radar Dataset - *LRR-Sim*

Our Doppler-Driven aggregation method addresses the increasing sparsity of radar point clouds at long ranges, therefore we are particularly interested in evaluating its performance at long distances. Existing radar point cloud datasets cover short and medium range distances, reaching up to 175m [25]. However, there is a gap in datasets for long-range automotive radar [1, 2, 5, 34], which can detect up to 300m, a range critical for autonomous driving on highways and at high speeds [23, 36, 48]. Obtaining accurate annotations beyond 175m is challenging, as the radar’s point cloud becomes very sparse at these distances, and typical LIDAR and camera sensors used for annotations lack this range. To address this, we introduce a long-range radar dataset with point clouds up to 300m and accurate annotations generated via radar simulation, building on prior work that demonstrates the realism and reliability of simulated radar data [7].

The simulation models a high-end, long-range radar in highway scenarios. Automotive scenarios were generated in CARLA [12] using CARLA highway environment maps,

and converted to radar point clouds using a physical model of a 77GHz MIMO radar with 12 transmit and 16 receive antennas. The radar’s received signal was computed via ray tracing between the radar antennas and objects in the scene, followed by range-Doppler 2D FFT and azimuth-elevation beamforming to obtain the reflection intensity spectrum. Point clouds were then extracted from this spectrum using the CFAR algorithm [32]. Additional implementation details are provided in Appendix E.

We refer to the long-range radar simulation dataset as *LRR-Sim*. It includes 42 training and 8 testing highway scenarios, each lasting approximately 30 seconds at 20 frames per second, resulting in 18,172 training frames and 3,363 testing frames. Vehicle types include cars, trucks, and vans, with an average of 7.3 vehicles per frame and a total of  $\sim 160K$  vehicle instances with  $\sim 28K$  beyond 175m. The point cloud extends up to 300m with a field of view of  $\pm 55^\circ$  in azimuth, and  $\pm 20^\circ$  in elevation. All vehicles within this range and field of view are accurately annotated with 3D bounding boxes. For more details on *LRR-Sim* and example demonstrations, please refer to our GitHub<sup>1</sup>. We hope this dataset serves as a valuable resource for advancing radar research, including applications beyond the scope of this paper.

## 6. Results

We evaluate the performance improvement of object detection when using *DoppDrive* as a preprocessing step with four radar-based detection networks across three datasets, covering diverse conditions and settings. The radar detection networks include Radar PillarNet (RPNNet) [47], based on PointPillars [20]; SMURF (SMF) [22], which enhances PointPillars with kernel density estimation; Nvradarnet (NVR) [29], a 2D convolutional Feature Pyramid Network in bird’s-eye view; and K-Radar (KRD) [27], which utilizes 3D sparse convolution. Implementation details are provided in Appendix F.

We selected datasets with large detection ranges to highlight the role of aggregation in addressing long-range sparsity, and with varying point cloud densities due to differences in radar resolution. Tab. 2 compares the datasets used in our evaluation. aiMotive has the lower angular resolution and sparsest point cloud compared to RADIAL and *LRR-Sim*; all are sparser than LiDAR. Detection ranges reach up to 175m for aiMotive, 103m for RADIAL, and 300m for *LRR-Sim*, meeting the requirements for long-range automotive radar [1, 2, 5, 23, 34, 36, 48]. Velocity sources also differ: aiMotive uses INS-GPS, RADIAL lacks accurate INS and uses radar-based estimation, and *LRR-Sim* provides ground-truth from simulation. The datasets span diverse

---

<sup>1</sup>The *LRR-Sim* dataset is available at: <https://github.com/yuvalHG/LRRSim>

scenarios: RADIAL includes city, countryside, and highway scenes; aiMotive covers urban and highway; and *LRR-Sim* focuses on highways.

In all tests, we set the tolerance disparity distance to  $\mathcal{D} = 2m$  to limit the aggregation duration in *DoppDrive*. This value was empirically found to give the best results, as detailed in Sec. 6.3. We compare *DoppDrive* with two reference methods: (1) standard aggregation, which combines points from frames up to  $0.7s$  in the past with ego-vehicle motion compensation, an empirically optimized duration for best performance; and (2) no aggregation. In both references, unless specified otherwise, the ego-speed Doppler component is removed from the point cloud Doppler measurements. This aids object detection by distinguishing reflections from static objects (near-zero Doppler) and dynamic objects (non-near-zero Doppler).

We evaluated object detection performance using average precision (AP), the integral of the precision-recall curve, for the 'vehicle' class, which includes cars, trucks, vans, and buses. Detection accuracy is measured by 2D bounding box IOU in birds-eye-view between detections and ground truth, using a 0.1 threshold. While aiMotive and *LRR-Sim* provide bounding box annotations, RADIAL offers only a single point on the object's front-facing contour. To enable consistent evaluation, we assigned a fixed-size bounding box—based on average vehicle dimensions—so that its front edge aligns with the provided point, assuming zero heading angle.

### 6.1. Object Detection Performance Gain

Tab. 1 compares the performance of the four selected object detection methods across three datasets, all detailed in Sec. 6. The evaluation uses three types of point cloud inputs: (1) single-frame reflection points without aggregation, (2) standard aggregation with ego-motion compensation, and (3) our Doppler-driven aggregation method, *DoppDrive*. For all methods, ego-speed Doppler components were removed from the Doppler measurements, and the input features of each point included the  $x, y, z$  coordinates, Doppler, reflection intensity, and time index for aggregated inputs. The results show that both aggregation methods outperform single-frame detection, with Doppler-driven aggregation achieving a greater improvements over standard aggregation across all detectors and datasets. The largest performance gain is observed on the aiMotive dataset, likely due to its radar's lower angular resolution and sparser point cloud compared to the other datasets. Because the point cloud is more sparse, it benefits more from *DoppDrive*'s aggregation, which increases its density with minimal scatter. Notably, the performance improvement is evident not only when precise ego-vehicle velocity is provided by GPS-INS (aiMotive) or simulation (*LRR-Sim*) but also when the velocity is estimated directly from the radar point cloud

(RADIAL). Among the four detectors compared, SMF [22] and KRD [27] achieve the highest performance, both with and without aggregation. Qualitative examples demonstrating *DoppDrive*'s effectiveness appear in Fig. 2 and in Appendix A.

To analyze the performance gains, we present an ablation study in Tab. 3 using the aiMotive dataset and SMF [22] detector, assessing the contributions of each component in *DoppDrive* as outlined in the table columns: (1) Ego-vehicle velocity compensation in aggregation (Ego. agg.), (2) GPS-INS ego-vehicle velocity measurement or radar-based estimation (GPS-INS Vel.), (3) Ego-speed Doppler component removal (Ego-Dopp.), (4) radial motion compensation using Eq. (6) (Radial Comp.), and (5) tangential spread mitigation by limiting aggregation duration based on Eq. (11) (Non-fix Duration).

The ablation test shows that both radial compensation and variable aggregation durations per point contribute to *DoppDrive*'s performance gains (rows 6 vs. 5, and 8 vs. 6, respectively). It also shows that using the ego-vehicle velocity estimated from the radar point cloud, instead of the GPS-INS velocity measurement, results in a relatively small performance degradation for *DoppDrive* (row 7 vs. 8).

### 6.2. Long Range Detection Performance

In this section, we evaluate *DoppDrive* at long ranges ( $175m$ - $300m$ ), where the point cloud is highly sparse. Detecting objects at these distances is crucial for high-speed autonomous driving. Since datasets like aiMotive and RADIAL are limited to  $175m$ , we use *LRR-Sim* (Sec. 5), which provides simulated long-range radar data with accurate annotations up to  $300m$ .

Tab. 4 shows detection performance on *LRR-Sim* for objects within  $175m$ - $300m$  using four object detectors from Sec. 6. We compare three input types: *DoppDrive*, standard aggregation with ego-motion compensation, and no aggregation, with the ego-speed Doppler component removed in all cases. Compared to the full-range results in Tab. 1, accuracy drops significantly at longer distances, but *DoppDrive* retains and even enhances its advantage. This improvement at longer ranges is due to the sparser point cloud, where increased density from temporal aggregation with minimal scatter proves even more beneficial.

### 6.3. Optimization of the Dispersion Tolerance $\mathcal{D}$

We perform an ablation study on *DoppDrive*'s hyperparameter  $\mathcal{D}$ , which defines the tolerated average position offset during aggregation and controls the aggregation duration for each point. Tab. 5 shows the average precision performance of the SMF [22] object detection network with the *LRR-Sim* dataset for different values of  $\mathcal{D}$ . The results indicate that the best performance was achieved with  $\mathcal{D} = 2m$ , which was used for all tests presented in the paper.

Method	aiMotive				Radial				LRR-Sim			
	SMF	KRD	RPNNet	NVR	SMF	KRD	RPNNet	NVR	SMF	KRD	RPNNet	NVR
No Agg.	74.6	75.0	73.4	70.9	91.3	91.4	91.0	89.3	89.2	88.7	88.7	86.6
Standard Agg.	81.7	82.3	80.2	75.2	92.5	92.1	92.3	91.2	91.1	89.9	90.8	90.1
<i>DoppDrive</i>	<b>89.1</b>	<b>89.4</b>	<b>87.8</b>	<b>81.8</b>	<b>95.8</b>	<b>95.5</b>	<b>95.7</b>	<b>94.1</b>	<b>93.3</b>	<b>93.1</b>	<b>92.9</b>	<b>92.7</b>

Table 1. Average Precision (AP) of four detectors: SMURF (SMF) [22], K-Radar (KRD) [27], Radar PillarNet (RPNNet) [47], and Nvradar-net (NVR) [29]. Results are evaluated across three datasets (aiMotive, Radial, LRR-Sim) with no aggregation, standard aggregation with ego-vehicle motion compensation, and *DoppDrive*.

	aiMotive	RADial	LRR-Sim
Resolution	Low	High	High
Range	175m	103m	300m
FOV	$\pm 16^\circ$	$\pm 90^\circ$	$\pm 55^\circ$
Ego-vel	INS-GPS	Radar	Simulation
FPS	18	5	20
# Train	21402	5450	18172
# Test	5181	1873	3363
# 3D Boxes	427K	9.5K	160K

Table 2. Comparison of the three tested datasets by angular resolution (Resolution), point cloud maximal range (Range), azimuth field-of-view (FOV), ego-vehicle velocity source (Ego-vel), frame rate (FPS), the number of frames in the training (# Train) and test (# Test) sets, and number of objects (# 3D Boxes).

ID	Ego. agg.	GPS-INS Vel.	Ego-Dopp.	Radial Comp.	Non-fix Duration	AP
1	✗	-	✗	✗	✗	66.3
2	✗	✗	✓	✗	✗	73.1
3	✗	✓	✓	✗	✗	74.8
4	✓	✓	✗	✗	✗	76.1
5	✓	✓	✓	✗	✗	81.4
6	✓	✓	✓	✓	✗	85.2
7	✓	✗	✓	✓	✓	87.7
8	✓	✓	✓	✓	✓	<b>89.1</b>

Table 3. Ablation study of *DoppDrive* components: Average Precision (AP) on aiMotive dataset with SMF detector [22].

Method	SMF	KRD	RPNNet	NVR
No Agg.	61.2	61.5	61.8	60.7
Standard Agg.	63.1	64.1	62.7	61.3
<i>DoppDrive</i>	<b>69.2</b>	<b>68.9</b>	<b>68.6</b>	<b>66.9</b>

Table 4. Average Precision at range  $> 175m$  on the *LRR-Sim* dataset with four detectors: SMF [22], K-Radar (KRD) [27], RPNNet [47], and Nvradar-net (NVR) [29].

## 6.4. Point Elimination Evaluation

*DoppDrive* shortens integration duration to filter out points with high tangential dispersion, resulting in point elimina-

$\mathcal{D}$ [m]	1	2	3	4	5
AP	91.2	<b>93.3</b>	92.5	92.3	89.6

Table 5. Average precision (AP) of SMF [22] on the *LRR-Sim* dataset as a function of the aggregation displacement tolerance  $\mathcal{D}$ .

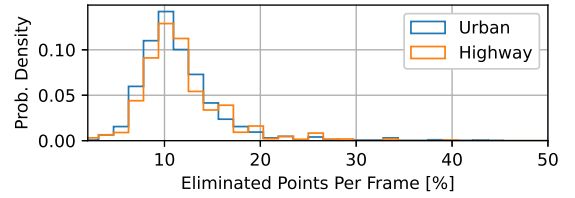


Figure 5. Point elimination in urban and highway (aiMotive)

tion compared to fixed-duration aggregation. Fig. 5 shows that *DoppDrive* removes an average of 11% of dynamic points per frame, relative to fixed-duration aggregation, in aiMotive’s urban and highway scenes, with most frames exhibiting less than 20% elimination. This yields a 3.9-point AP gain (rows 8 vs. 6 in Tab. 3), demonstrating that even modest elimination improves performance. A detailed breakdown of point elimination is provided in Appendix C.

## 7. Conclusion

In this paper, we present *DoppDrive*, a novel method to enhance radar point cloud density before object detection with minimal scatter by leveraging Doppler information in temporal aggregation. *DoppDrive* reduces scatter from dynamic objects by adjusting previous frames’ points in the radial direction based on their dynamic Doppler components and by limiting each point’s aggregation duration according to its specific parameters. An ablation study validated the contribution of both elements, while complexity analysis showed minimal computational overhead. *DoppDrive*’s enhanced point cloud improves object detection performance, as demonstrated across four detectors and three datasets.

Additionally, we introduce *LRR-Sim*, a long-range radar simulation dataset with sparse point clouds resulting from extended detection ranges, and precise annotations up to 300m, significantly beyond existing datasets. The dataset is publicly available to support advancements in long-range radar detection, which is essential for high-speed autonomous driving.



## References

- [1] Continental AG. Advanced radar sensor ar540. <https://www.continental-automotive.com/en/components/radars/long-range-radars/advanced-radar-sensor-ar540.html>. Accessed: Nov. 10, 2024. 2, 6, 13
- [2] ZF Friedrichshafen AG. Automated driving functions: Zf captures contract for 4d full-range radar with chinese oem, 2021. Accessed: Nov. 11, 2024. 2, 6, 13
- [3] Simegnew Yihunie Alaba. Gps-imu sensor fusion for reliable autonomous vehicle position estimation. *arXiv preprint arXiv:2405.08119*, 2024. 2, 3
- [4] Yasin Almalioglu, Mehmet Turan, Chris Xiaoxuan Lu, Niki Trigoni, and Andrew Markham. Milli-rio: Ego-motion estimation with low-cost millimetre-wave radar. *IEEE Sensors Journal*, 21(3):3314–3323, 2020. 2, 3
- [5] Aptiv. Radars — advanced safety. <https://www.aptiv.com/en/solutions/advanced-safety/adas/radars>. Accessed: Nov. 11, 2024. 2, 6, 13
- [6] Jie Bai, Lianqing Zheng, Sen Li, Bin Tan, Sihan Chen, and Libo Huang. Radar transformer: An object classification network based on 4d mmw imaging radar. *Sensors*, 21(11): 3854, 2021. 3
- [7] Oded Bialer and Yuval Haitman. Radsimreal: Bridging the gap between synthetic and real data in radar object detection with simulation. In *Proceedings of the IEEE/CVF Conference on Computer Vision and Pattern Recognition*, pages 15407–15416, 2024. 6
- [8] Holger Caesar, Varun Bankiti, Alex H Lang, Sourabh Vora, Venice Erin Liong, Qiang Xu, Anush Krishnan, Yu Pan, Giancarlo Baldan, and Oscar Beijbom. nuscenes: A multi-modal dataset for autonomous driving. In *Proceedings of the IEEE/CVF conference on computer vision and pattern recognition*, pages 11621–11631, 2020. 3
- [9] Averil B Chatfield. *Fundamentals of high accuracy inertial navigation*. American Institute of Aeronautics and Astronautics, 1997. 2, 3
- [10] Jean-Luc Déziel, Pierre Merriault, Francis Tremblay, Dave Lessard, Dominique Plourde, Julien Stanguennec, Pierre Goulet, and Pierre Olivier. Pixset: An opportunity for 3d computer vision to go beyond point clouds with a full-waveform lidar dataset. In *2021 IEEE International Intelligent Transportation Systems Conference (ITSC)*, pages 2987–2993. IEEE, 2021. 3
- [11] Xu Dong, Pengluo Wang, Pengyue Zhang, and Langechuan Liu. Probabilistic oriented object detection in automotive radar. In *Proceedings of the IEEE/CVF Conference on Computer Vision and Pattern Recognition Workshops*, pages 102–103, 2020. 1
- [12] Alexey Dosovitskiy, German Ros, Felipe Codevilla, Antonio Lopez, and Vladlen Koltun. Carla: An open urban driving simulator. In *Conference on robot learning*, pages 1–16. PMLR, 2017. 6, 13
- [13] Jay Farrell and Matthew Barth. The global positioning system and inertial navigation. (*No Title*), 1999. 2, 3
- [14] Felix Fent, Philipp Bauerschmidt, and Markus Lienkamp. Radargnn: Transformation invariant graph neural network for radar-based perception. In *Proceedings of the IEEE/CVF Conference on Computer Vision and Pattern Recognition*, pages 182–191, 2023. 1, 3
- [15] Luigi Giuffrida, Guido Masera, and Maurizio Martina. A survey of automotive radar and lidar signal processing and architectures. *Chips*, 2(4):243–261, 2023. 1
- [16] Yuval Haitman and Oded Bialer. BoostRAD: Enhancing object detection by boosting radar reflections. In *Proceedings of the IEEE/CVF Winter Conference on Applications of Computer Vision*, pages 1638–1647, 2024. 1
- [17] Henry Alexander Ignatious, Manzoor Khan, et al. An overview of sensors in autonomous vehicles. *Procedia Computer Science*, 198:736–741, 2022. 1
- [18] Dominik Kellner, Michael Barjenbruch, Jens Klappstein, Jürgen Dickmann, and Klaus Dietmayer. Instantaneous ego-motion estimation using doppler radar. In *16th International IEEE Conference on Intelligent Transportation Systems (ITSC 2013)*, pages 869–874. IEEE, 2013. 2, 3
- [19] Woosuk Kim, Hyunwoong Cho, Jongseok Kim, Byungkwan Kim, and Seongwook Lee. Yolo-based simultaneous target detection and classification in automotive fmcw radar systems. *Sensors*, 20(10):2897, 2020. 1
- [20] Alex H Lang, Sourabh Vora, Holger Caesar, Lubing Zhou, Jiong Yang, and Oscar Beijbom. Pointpillars: Fast encoders for object detection from point clouds. In *Proceedings of the IEEE/CVF conference on computer vision and pattern recognition*, pages 12697–12705, 2019. 3, 6
- [21] Tsung-Yi Lin, Piotr Dollár, Ross Girshick, Kaiming He, Bharath Hariharan, and Serge Belongie. Feature pyramid networks for object detection. In *Proceedings of the IEEE conference on computer vision and pattern recognition*, pages 2117–2125, 2017. 3
- [22] J Liu, Q Zhao, W Xiong, T Huang, QL Han, and B Zhu SMURF. Spatial multi-representation fusion for 3d object detection with 4d imaging radar., 2023. DOI: <https://doi.org/10.1109/TIV>, pages 1–14, 2023. 1, 2, 3, 6, 7, 8, 11, 12, 13, 14
- [23] Matt Markel. *Radar for Fully Autonomous Driving*. Artech House, 2022. 2, 6
- [24] Enrique Marti, Miguel Angel De Miguel, Fernando Garcia, and Joshue Perez. A review of sensor technologies for perception in automated driving. *IEEE Intelligent Transportation Systems Magazine*, 11(4):94–108, 2019. 1
- [25] Tamás Matuszka, Iván Barton, Ádám Butykai, Péter Hajas, Dávid Kiss, Domonkos Kovács, Sándor Kunsági-Máté, Péter Lengyel, Gábor Németh, Levente Pető, et al. aimotive dataset: A multimodal dataset for robust autonomous driving with long-range perception. *arXiv preprint arXiv:2211.09445*, 2022. 2, 3, 6
- [26] Michael Meyer and Georg Kuschik. Automotive radar dataset for deep learning based 3d object detection. In *2019 16th European Radar Conference (EuRAD)*, pages 129–132. IEEE, 2019. 3
- [27] Dong-Hee Paek, Seung-Hyun Kong, and Kevin Tirta Wijaya. Enhanced k-radar: Optimal density reduction to improve detection performance and accessibility of 4d radar tensor-based object detection. In *2023 IEEE Intelligent Ve-*

- icles Symposium (IV), pages 1–6. IEEE, 2023. 1, 3, 6, 7, 8, 14
- [28] Andras Palfy, Ewoud Pool, Srimannarayana Baratam, Julian FP Kooij, and Dariu M Gavrila. Multi-class road user detection with 3+ 1d radar in the view-of-delft dataset. *IEEE Robotics and Automation Letters*, 7(2):4961–4968, 2022. 1, 2, 3
- [29] Alexander Popov, Patrik Gebhardt, Ke Chen, and Ryan Oldja. Nvradarnet: Real-time radar obstacle and free space detection for autonomous driving. In *2023 IEEE International Conference on Robotics and Automation (ICRA)*, pages 6958–6964. IEEE, 2023. 1, 2, 3, 6, 8, 14
- [30] Matthias Rapp, Michael Barjenbruch, Klaus Dietmayer, Markus Hahn, and Jürgen Dickmann. A fast probabilistic ego-motion estimation framework for radar. In *2015 European Conference on Mobile Robots (ECMR)*, pages 1–6. IEEE, 2015. 2, 3
- [31] Julien Rebut, Arthur Ouaknine, Waqas Malik, and Patrick Pérez. Raw high-definition radar for multi-task learning. In *Proceedings of the IEEE/CVF Conference on Computer Vision and Pattern Recognition*, pages 17021–17030, 2022. 1, 3
- [32] Hermann Rohling. Radar cfar thresholding in clutter and multiple target situations. *IEEE transactions on aerospace and electronic systems*, (4):608–621, 1983. 1, 6, 14
- [33] Liat Sless, Bat El Shlomo, Gilad Cohen, and Shaul Oron. Road scene understanding by occupancy grid learning from sparse radar clusters using semantic segmentation. In *Proceedings of the IEEE/CVF International Conference on Computer Vision Workshops*, pages 0–0, 2019. 1
- [34] Bosch Mobility Solutions. Front radar sensor. <https://www.bosch-mobility.com/en/solutions/sensors/front-radar-sensor/>. Accessed: Nov. 11, 2024. 2, 6
- [35] James J Spilker Jr, Penina Axelrad, Bradford W Parkinson, and Per Enge. *Global positioning system: theory and applications, volume I*. American Institute of Aeronautics and Astronautics, 1996. 2, 3
- [36] Shunqiao Sun, Athina P Petropulu, and H Vincent Poor. Mimo radar for advanced driver-assistance systems and autonomous driving: Advantages and challenges. *IEEE Signal Processing Magazine*, 37(4):98–117, 2020. 2, 6
- [37] Peter Svenningsson, Francesco Fioranelli, and Alexander Yarovoy. Radar-pointgcn: Graph based object recognition for unstructured radar point-cloud data. In *2021 IEEE Radar Conference (RadarConf21)*, pages 1–6. IEEE, 2021. 3
- [38] Bin Tan, Zhixiong Ma, Xichan Zhu, Sen Li, Lianqing Zheng, Sihan Chen, Libo Huang, and Jie Bai. 3-d object detection for multiframe 4-d automotive millimeter-wave radar point cloud. *IEEE Sensors Journal*, 23(11):11125–11138, 2022. 1, 2, 3
- [39] Michael Ulrich, Sascha Braun, Daniel Köhler, Daniel Niederlöhner, Florian Faion, Claudius Gläser, and Holger Blume. Improved orientation estimation and detection with hybrid object detection networks for automotive radar. In *2022 IEEE 25th International Conference on Intelligent Transportation Systems (ITSC)*, pages 111–117. IEEE, 2022. 3
- [40] Baowei Xu, Xinyu Zhang, Li Wang, Xiaomei Hu, Zhiwei Li, Shuyue Pan, Jun Li, and Yongqiang Deng. Rpf-net: A 4d radar pillar feature attention network for 3d object detection. In *2021 IEEE International Intelligent Transportation Systems Conference (ITSC)*, pages 3061–3066. IEEE, 2021. 3
- [41] Bin Yang, Wenjie Luo, and Raquel Urtasun. Pixor: Real-time 3d object detection from point clouds. In *Proceedings of the IEEE conference on Computer Vision and Pattern Recognition*, pages 7652–7660, 2018. 3
- [42] Kadir Yilmaz, Jonas Schult, Alexey Nekrasov, and Bastian Leibe. Mask4former: Mask transformer for 4d panoptic segmentation. In *2024 IEEE International Conference on Robotics and Automation (ICRA)*, pages 9418–9425. IEEE, 2024. 1
- [43] Ekim Yurtsever, Jacob Lambert, Alexander Carballo, and Kazuya Takeda. A survey of autonomous driving: Common practices and emerging technologies. *IEEE access*, 8:58443–58469, 2020. 1
- [44] Ao Zhang, Farzan Erlik Nowruzi, and Robert Laganriere. Raddet: Range-azimuth-doppler based radar object detection for dynamic road users. In *2021 18th Conference on Robots and Vision (CRV)*, pages 95–102. IEEE, 2021. 1
- [45] Guoqiang Zhang, Haopeng Li, and Fabian Wenger. Object detection and 3d estimation via an fmcw radar using a fully convolutional network. In *ICASSP 2020-2020 IEEE International Conference on Acoustics, Speech and Signal Processing (ICASSP)*, pages 4487–4491. IEEE, 2020. 1
- [46] Lianqing Zheng, Zhixiong Ma, Xichan Zhu, Bin Tan, Sen Li, Kai Long, Weiqi Sun, Sihan Chen, Lu Zhang, Mengyue Wan, et al. Tj4dradset: A 4d radar dataset for autonomous driving. In *2022 IEEE 25th International Conference on Intelligent Transportation Systems (ITSC)*, pages 493–498. IEEE, 2022. 3
- [47] Lianqing Zheng, Sen Li, Bin Tan, Long Yang, Sihan Chen, Libo Huang, Jie Bai, Xichan Zhu, and Zhixiong Ma. Refusion: Fusing 4-d radar and camera with bird’s-eye view features for 3-d object detection. *IEEE Transactions on Instrumentation and Measurement*, 72:1–14, 2023. 3, 6, 8, 14
- [48] Taohua Zhou, Mengmeng Yang, Kun Jiang, Henry Wong, and Diange Yang. Mmw radar-based technologies in autonomous driving: A review. *Sensors*, 20(24):7283, 2020. 2, 6

# DoppDrive: Doppler-Driven Temporal Aggregation for Improved Radar Object Detection

## Supplementary Material

### A. Additional Qualitative Results

In this section, we provide qualitative examples supplementary to those shown in Fig. 2. Fig. 6 showcase an example from *LRR-Sim* dataset, while Figs. 7 and 8 present two examples from the aiMotive dataset. The layout follows the same structure as Fig. 2. For each example, the single-frame point cloud (without aggregation) is shown on the left, standard aggregation over 0.7s is displayed in the middle, and the results of *DoppDrive* are presented on the right. Reflection points from dynamic and static objects are plotted in blue and orange, respectively. Detected bounding boxes using SMF [22] are marked in blue, while ground truth bounding boxes are marked in pink.

In all the examples, it is evident that without aggregation, the reflection points are sparse, often with only one or two points per object, and sometimes none, leading to missed object detections. Standard aggregation results in significant scatter of reflection points from dynamic objects (blue points). In contrast, *DoppDrive* produces dense reflection points with minimal scatter, resulting in detections that are better aligned with the annotations compared to standard aggregation.

### B. Computational Complexity Evaluation

We next assess the computational overhead of *DoppDrive*, implemented according to Algorithm 1, with  $g(\theta)$  precomputed for each  $\theta$  and accessed via a lookup table. Tab. 6 compares the runtime of SMF [22] object detection with *DoppDrive* aggregation, standard aggregation, and no aggregation on an NVIDIA Tesla V100 SXM2 32 GB. The results show that *DoppDrive*'s aggregation time is significantly smaller than the detection time, contributing minimal runtime overhead and making it suitable for real-time applications. *DoppDrive* slightly reduces detector runtime compared to standard aggregation by aggregating fewer points due to its dynamic aggregation duration.

### C. Impact of Point Elimination

*DoppDrive* limits integration duration to suppress points with high tangential dispersion, resulting in point elimination relative to fixed-duration aggregation. This subsection evaluates the elimination rate and its impact on performance.

Tab. 7 breaks down the AP gains and the average percentage of eliminated dynamic points per frame—relative to fixed-duration aggregation with radial compensation (rows

Aggregation Method	Aggregation Time [ms]	Detection Time [ms]	Total Time [ms]
None	0	66.4	66.4
Standard	1.4	67.8	69.2
<i>DoppDrive</i>	2.0	67.5	69.5

Table 6. Runtime assessment of *DoppDrive* using the SMF detector [22]. The columns, from left to right, show the point cloud aggregation methods, aggregation runtime, object detection runtime with the aggregated points, and the total runtime, calculated as the sum of aggregation and detection runtimes.

Range [m]	[0, 40]	[40, 80]	[80, 120]	[120, 160]
Elim.%/AP Gain	16.6/5.6	12.4/4.6	10.9/2.9	10.5/2.7
Abs. Velocity [m/s]	[0, 12]	[12, 24]	[24, 36]	[36, 48]
Elim.%/AP Gain	10.6/3.7	11.1/4.3	11.8/4.9	12.6/5.3
Abs. Heading [°]	[0, 30]	[30, 60]	[60, 120]	[120, 180]
Elim.%/AP Gain	10.0/3.9	11.0/4.1	15.5/5.1	11.0/4.0

Table 7. Point elimination rate (blue) and AP gain (green) over radial compensation with fixed aggregation duration and no elimination, at different range, velocity, and heading intervals (aiMotive).

8 vs. 6 in Tab. 3)—across heading, velocity, and range bins. Elimination reaches up to 16%, increasing at short ranges, higher speeds, and more tangential headings. While the overall elimination rate is modest, it has a noticeable impact on performance, with larger gains observed at higher elimination levels.

### D. Calculation of $g(\theta_k^i)$

In Eq. (10), we provide the expression for  $g(\theta_k^i)$ , which is defined as:

$$g(\theta_k^i) = \mathbb{E}_{\alpha_k^i} [\tan(\theta_k^i + \alpha_k^i)] = \int_{-\pi/2}^{\pi/2} \tan(\theta_k^i + \alpha) f_{\alpha_k^i}(\alpha) d\alpha, \quad (12)$$

where  $f_{\alpha_k^i}(\alpha)$  represents the probability distribution function of the heading angle  $\alpha$ . In this section, we explain how to compute  $g(\theta_k^i)$  as defined by Eq. (12).

Fig. 9 shows the probability density function (PDF) of  $\alpha$ , derived from annotations in the aiMotive dataset. The distribution is sharply concentrated around zero, with significantly smaller secondary peaks near  $\pm 90^\circ$ . To model this distribution, we fit a truncated Laplace distribution:

$$f_{\alpha_k^i}(\alpha) = \frac{1}{2b} \exp\left(-\frac{|\alpha - \mu|}{b}\right), \quad \alpha \in [-\pi/2, \pi/2], \quad (13)$$

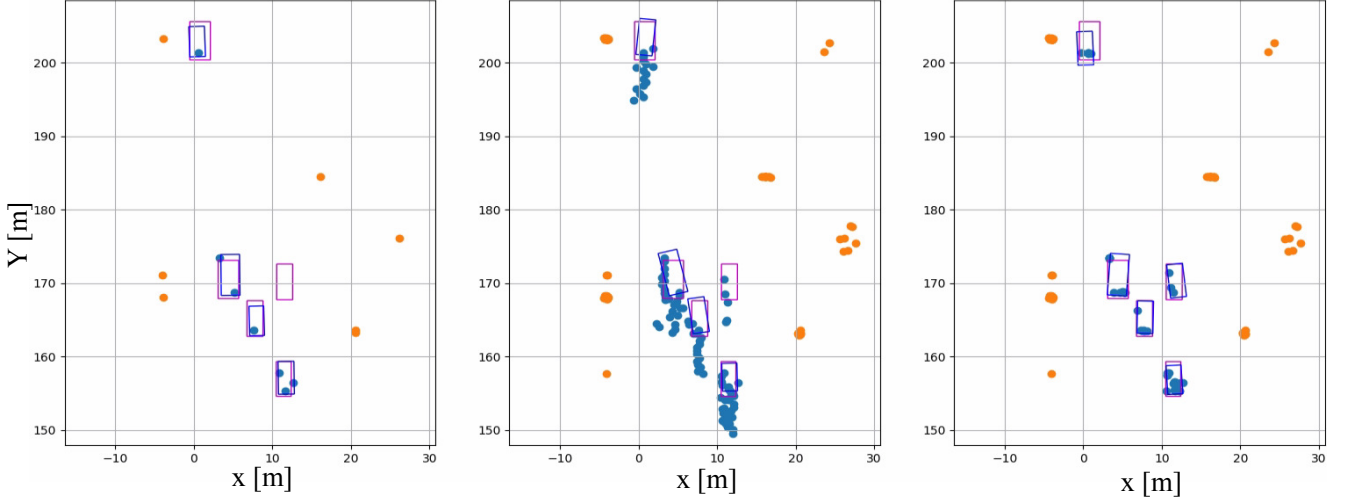


Figure 6. Qualitative example from *LRR-Sim* shown in bird’s-eye view. The point cloud of dynamic objects is shown in blue, while that of static objects is shown in orange. SMF [22] detections are represented by blue bounding boxes, and ground truth bounding boxes are shown in pink. The left figure depicts results without aggregation, the middle figure shows standard aggregation with ego-motion compensation, and the right figure shows the results of *DoppDrive*.

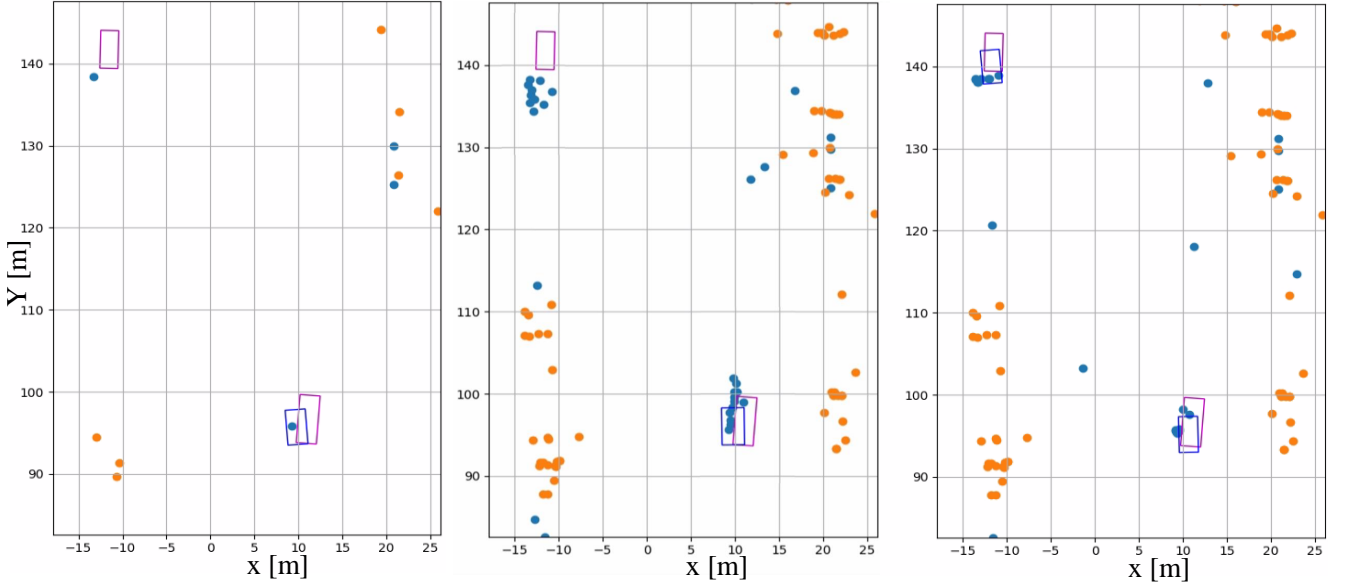


Figure 7. Qualitative example from *aiMotive* shown in bird’s-eye view. The point cloud of dynamic objects is shown in blue, while that of static objects is shown in orange. SMF [22] detections are represented by blue bounding boxes, and ground truth bounding boxes are shown in pink. The left figure depicts results without aggregation, the middle figure shows standard aggregation with ego-motion compensation, and the right figure shows the results of *DoppDrive*.

where we set  $\mu = 0$  and  $b = 3.1$ . The minor peaks near  $\pm 90^\circ$  were neglected in this approximation. The fitted Laplace distribution is plotted in black in Fig. 9. As shown, it aligns well with the main mode of the empirical distribution.

Based on this, the integral in Eq. (12) can be evaluated numerically, either using the empirical histogram or

the Laplace approximation for  $f_{\alpha_k^i}(\alpha)$ . For the experiments in the main paper, we used the Laplace approximation to precompute  $g(\theta_k^i)$  over a grid of  $\theta_k^i$  values and stored the results in a look-up table for efficient use in Algorithm 1.

Using the full multi-modal histogram of  $\alpha$  from Fig. 9 to compute the integral numerically yielded a slight performance improvement. Specifically, the SMF detector [22]



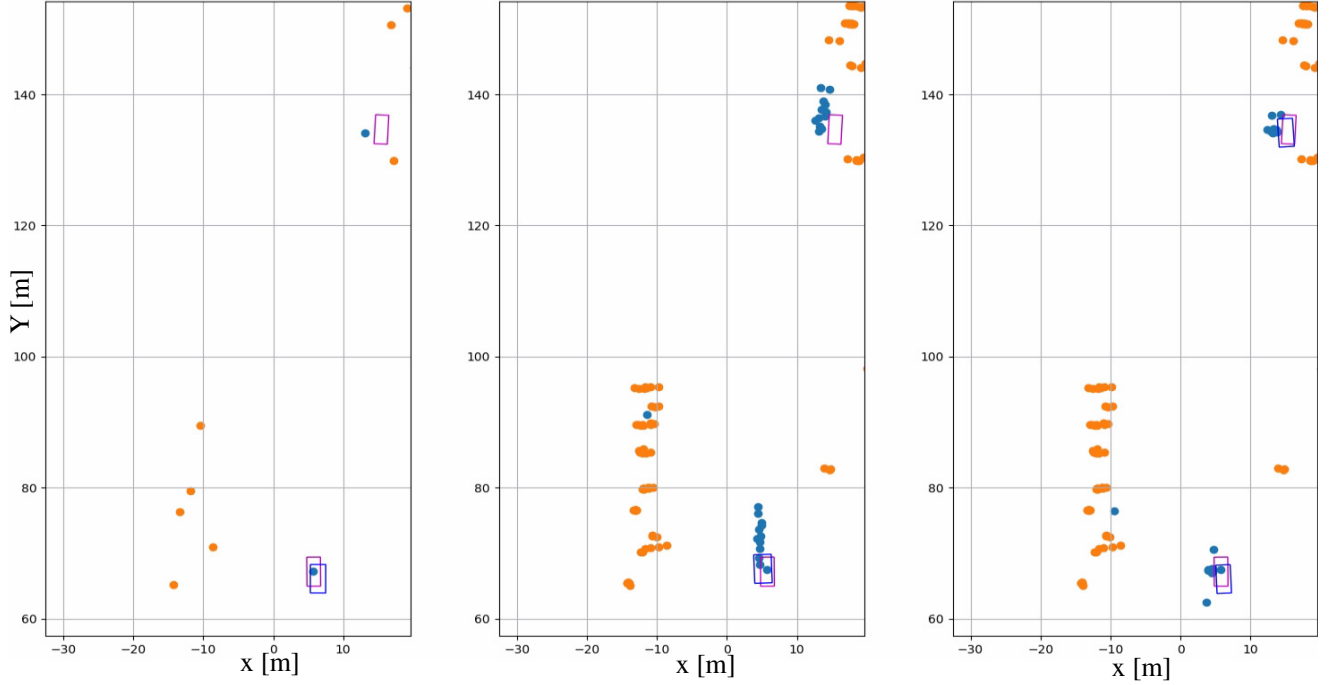


Figure 8. Qualitative example from aiMotive shown in bird’s-eye view. The point cloud of dynamic objects is shown in blue, while that of static objects is shown in orange. SMF [22] detections are represented by blue bounding boxes, and ground truth bounding boxes are shown in pink. The left figure depicts results without aggregation, the middle figure shows standard aggregation with ego-motion compensation, and the right figure shows the results of *DoppDrive*.

achieved a 0.4-point increase in Average Precision on the aiMotive dataset.

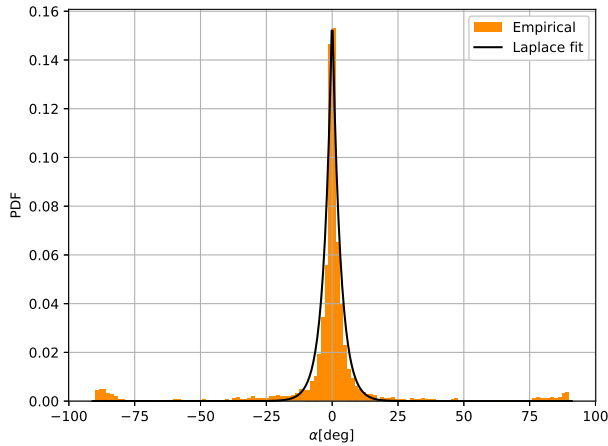


Figure 9. Probability distribution function (PDF) of reflection points’ heading directions used in calculating  $g(\theta_k^i)$ . The empirical PDF from aiMotive dataset annotations is shown in orange, with the Laplace distribution fit plotted in black.

## E. Supplementary Details on *LRR-Sim*

In this section, we provide additional details about *LRR-Sim*, the Long-Range Radar Simulation dataset introduced in Sec. 3. *LRR-Sim* focuses on highway scenarios with long-range vehicles of three types: ‘car,’ ‘van,’ and ‘truck’. The number of vehicles as a function of range in the dataset is presented in Fig. 10, which indicating that vehicle ranges extend up to 300m, with 17.5% of the vehicles located beyond 175m. The distribution of vehicle types in the dataset is illustrated in Fig. 11. It is observed that 65.7% of the vehicles are of type ‘car,’ representing relatively small-sized vehicles, while 17.9% are medium-sized ‘vans,’ and 16.5% are large vehicles of type ‘truck.’

The specifications of the simulated radar are detailed in Tab. 8. These specifications align with those of high-end long-range automotive radars [1, 2, 5], offering a detection range of up to 300m and high resolution in range, angle, and Doppler.

The simulated radar features 12 transmit and 16 receive antennas and uses a fast chirp FMCW waveform. The highway environment and vehicles were modeled using the CARLA simulation platform [12], incorporating dense reflection points from objects. Ray tracing was performed to compute interactions between the antennas and reflection points in the environment. The received signal at each an-

tenna was the sum of the transmitted waveforms echoed by all reflection points in the scene, with adjustments for intensity and delay determined by each reflection point's intensity and distance. To obtain the radar reflection intensity spectrum in the range, Doppler, and angle dimensions, standard radar signal processing techniques were applied to the received signals. This included range FFT, Doppler FFT, and azimuth-elevation beamforming. Finally, the radar point cloud was generated by identifying spectrum peaks that exceeded a local noise threshold, using the CFAR algorithm [32]. A video demonstration of *LRR-Sim* is included in our GitHub<sup>2</sup>.

Radar parameter	
Maximal range	300m
Range resolution	0.15m
Azimuth field of view	$\pm 55^\circ$
Azimuth resolution	1.2°
Elevation field of view	$\pm 20^\circ$
Elevation resolution	2°
Doppler resolution	0.13m/s
Doppler range	$[-80, 30]m/s$

Table 8. Specifications of radar used in *LRR-Sim*

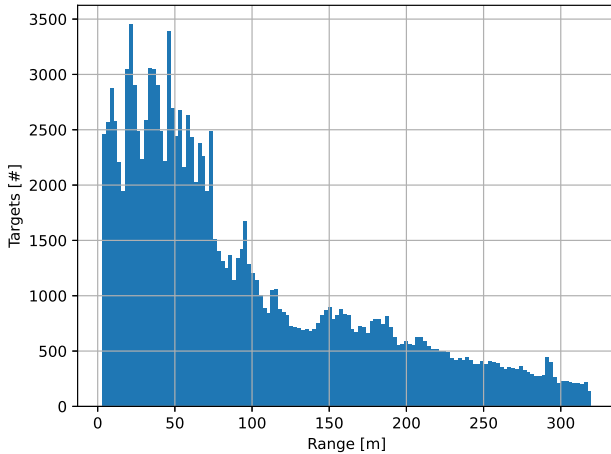


Figure 10. Number of vehicles by range in the *LRR-Sim* dataset.

## F. Detectors Implementation Details

For the performance evaluation of *DoppDrive* in Sec. 6, we used four detectors: Radar PillarNet (RPNet) [47], SMURF (SMF) [22], Nvradarnet (NVR) [29], and K-Radar (KRD) [27]. Details of their implementation are outlined below. For all methods, ego-speed Doppler components

<sup>2</sup>The *LRR-Sim* dataset is available at: <https://github.com/yuvalHG/LRRSim>

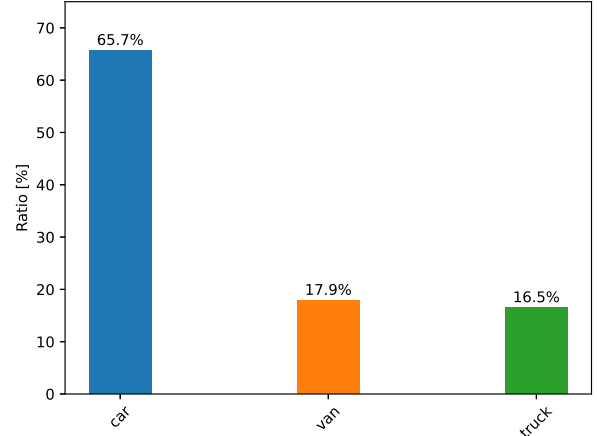


Figure 11. Distribution of vehicle types in the *LRR-Sim* dataset.

were removed from the Doppler measurements, and the input features for each point included the  $x, y, z$  coordinates, Doppler, reflection intensity, and time index for aggregated inputs. RPNet, SMF, and NVR used a  $0.25m \times 0.25m$  input grid resolution in the X-Y plane, while KRD employed a  $0.4m \times 0.4m \times 0.4m$  3D grid resolution. Three anchor sizes were used to cover small, medium, and large vehicles, each with two orientations:  $0^\circ$  and  $90^\circ$ . For SMF, we used two KDE blocks with bandwidths  $R1 = 1m$  and  $R2 = 2m$ . We apply radar point cloud augmentations, including flips, slight zoom in/out, and intensity jitter. Translations and rotations were excluded to prevent misalignment of Doppler measurements.

## G. Vertical Velocity Extension

In automotive scenarios, vertical displacement over short aggregation durations is typically negligible. Therefore, in deriving *DoppDrive*, we assume zero vertical velocity and focus solely on longitudinal and lateral motion. However, *DoppDrive* can be extended to account for vertical velocity if required. In this case, only the duration constraint in line 8 of Algorithm 1 is affected. The function  $g$  would be updated to incorporate elevation angle and vertical heading distribution, mitigating dispersion in both vertical and tangential directions.